CrossMark

The comparative study of two reusable phosphotungstic acid salts/reduced graphene oxides composites with enhanced photocatalytic activity

Junhong Li[1] · Lijun Luo[1] · Wei Tan[1] · Hongbin Wang[1] · Min Yang[1] · Fengzhi Jiang[2] · Wenrong Yang[3]

Abstract

In this work, two recyclable phosphotungstic acid salts/reduced graphene oxides were successfully prepared. The prepared samples were characterized by X-ray diffraction analysis (XRD), scanning electron microscopy (SEM), transmission electron microscopy (TEM), infrared spectroscopy (IR), X-ray photoelectron spectroscopy (XPS), thermo-gravimetric analysis (TGA), Raman spectroscopy, and photoluminescence spectroscopy (PL). The structure and catalytic performance of two composites were comparatively investigated, and the reduced graphene oxide mass ratios in $K_3[PW_{12}O_{40}]$/reduced graphene oxide (denoted as KPW-RGO) and $(NH_4)_3[PW_{12}O_{40}]$/reduced graphene oxide (denoted as NH4PW-RGO) were optimized and their roles in them were explored. The results indicate that the Keggin structures of KPW and NH4PW are still kept after being anchored on the RGO surface, but their morphologies change a lot in composites. The photocatalytic activities of KPW-3RGO (0.01989 min^{-1}) are 5.42 times than that of KPW (0.00367 min^{-1}), and NH4PW-1RGO (0.0184 min^{-1}) is 2.26 times than that of NH4PW (0.00814 min^{-1}). The enhanced photocatalytic activity is mainly ascribed to photo-induced interfacial charge transfer on the heterojunction between RGO and NH4PW or KPW and strong adsorption ability of RGO towards MO. Moreover, NH4PW-1RGO and KPW-3RGO had much better photocatalytic activity, good recyclable ability, and stability compared to HPW-RGO, which cannot be recycled.

Keywords Photocatalysis · Phosphotungstate · Reduced oxide graphene · Methyl orange

Introduction

In the recent decades, semiconductor-based photocatalysis has been considered as one of the promising techniques to

✉ Lijun Luo
10501931@qq.com

✉ Hongbin Wang

[1] Key Laboratory of Resource Clean Conversion in Ethnic Regions, Education Department of Yunnan, School of Chemistry and Environment, Yunnan MinZu University, Kunming 650500, People's Republic of China

[2] Key Laboratory of Medicinal Chemistry for Natural Resource, Ministry of Education, School of Chemical Science and Technology, Yunnan University, Kunming 650091, People's Republic of China

[3] Centre for Chemistry and Biotechnology, School of Life and Environmental Sciences, Deakin University, Waurn Ponds, Victoria 3216, Australia

challenge the worldwide energy shortage and environmental pollution issue (Moniz et al. 2015, Pelaez et al. 2012). It is also recognized as a supplementary technique for conventional biological treatment to remove recalcitrant and non-biodegradable micro-pollutants (Marsolek et al. 2014), and it is also one of the potential techniques to treat dye or pharmaceuticals wastewater with a high concentration (Chowdhury and Balasubramanian 2014, Kanakaraju et al. 2013). TiO2 remains the most suitable semiconductor choice for its great capability to degrade contaminants, high stability, and cost-effectiveness (Linsebigler et al. 1995). It can decompose organic pollutants into CO_2 and H_2O using solar energy. However, the rapid recombination of photogenerated electron-hole pairs and narrow light response range restrict its practical applications in wastewater treatment. Therefore, it is significantly important and necessary to explore and investigate new types of photocatalysts with extraordinary performance, excellent visible-light response, and good recyclability.

Heteropoly acids (HPAs), especially those with Keggin structure ($H_3PMo_{12}O_{40}$, $H_3PW_{12}O_{40}$, and $H_4SiW_{12}O_{40}$), have been widely investigated as favorable catalysts in degradation

of organic halides, dyes, and pesticides due to their excellent redox properties, good chemical stability, nontoxicity, and low cost (Antoniadis et al. 2010, Hori et al. 2008, Kormali et al. 2007, Troupis et al. 2009). However, traditional heteropoly acids with high solubility in polar solvents would impede recovery and reuse in industrial application. Moreover, the low surface area would restrict their catalytic activity. In order overcome these disadvantages, the researchers immobilized the HPAs onto the supports including activated carbon (Xiao et al. 2014), alumina (Méndez et al. 2011), amine-functionalized metal-organic framework (Wang et al. 2014), mesoporous silica (Feng et al. 2012, Luo et al. 2014a, Zhao et al. 2013), and mesoporous graphitic carbon nitride (Zhu et al. 2015), which can improve certain recycled ability and photocatalytic activity. Researchers also combined heteropoly acids with large mono-valent cations including K^+, Rb^+, Cs^+, and NH_4^+ to form insoluble salts with good recyclability (Corma et al. 1996, Holclajtner-Antunović et al. 2010, Liu et al. 2016).
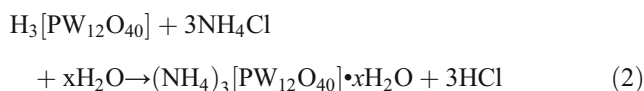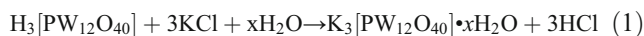
Since 2009, graphene has been considered as a good support of photocatalysts to improve adsorption ability and performance of photocatalysts for target pollutant removal (Chowdhury and Balasubramanian 2014, Ji et al. 2014, Morales-Torres et al. 2012, Yang et al. 2017) because of its exceptionally high specific surface area (Meyer et al. 2007), excellent conductivity (Khai et al. 2013), and good adsorption ability for organic pollutants (Xu et al. 2012). Liu and co-workers used the low-cost phosphotungstic acid loaded on gamma-aminopropyltriethoxysilane-coated graphene oxide (Liu et al. 2013). Tessonnier dispersed the polyoxometalates ($H_3PMo_{12}O_{40}$, $H_3PW_{12}O_{40}$, and $H_4PMo_{11}VO_{40}$) to oxygen- and alkyl-functionalized graphene sheets. Zhang group synthesized Keggin-type polyoxometalates (PMo11V)/reduced graphene oxide nanocomposites film via layer-by-layer self-assembly method (Zhang et al. 2017). Kooti group prepared graphene/$MnFe_2O_4$@$H_3PW_{12}O_{40}$ composites with the magnetic separable ability (Kooti et al. 2018). In the previous work, we also anchored $H_3PW_{12}O_{40}$ onto reduced graphene oxide to improve its adsorption ability and photocatalytic degradation ability for MO greatly (Xia et al. 2017). However, the polyoxometalate component in composites has no recyclability or will be lost during the usage process even it has been anchored onto separable magnetic materials due to the soluble nature. Hence, in this work, in order to obtain good recyclability, stability, and improve photocatalytic activity for this type of photocatalysts, we anchored two insoluble heteropoly acid salts (K_3[$PW_{12}O_{40}$-reduced graphene oxide] (denoted as KPW-RGO) and (NH_4)$_3$[$PW_{12}O_{40}$-reduced graphene oxide] (denoted as NH_4PW-RGO)) to reduced graphene oxide (RGO). The crystal phase structure, morphology, and chemical composition of two kinds of composites were comparatively investigated in detail. Most importantly, the roles of RGO in these two composites (NH_4PW-RGO and KPW-RGO) were also comparatively investigated in order to probe

the contribution of RGO in two composites for the target pollutant removal.

Experimental

Preparation of KPW-RGO and NH₄PW-RGO

Graphite oxide was prepared by oxidizing natural flake graphite powder (325 mesh) using the Hummers method (Hummers 1958, Stankovich et al. 2006). Two milligrams per milliliter of graphene oxide (GO) was obtained by ultrasonic treatment of self-made graphite oxide (0.60 g) in 300 mL of a mixture of water-ethanol (2:1) for 6 h and centrifugation at 4000 rpm for 15 min. The supernatant (GO) was collected and stored in a fridge for the following usage. The KPW-RGO and NH₄PW-RGO materials were synthesized via hydrothermal method. In the typical preparation process of KPW-RGO (NH₄PW-RGO) containing different mass ratios of RGO, firstly, 1.985 g of $H_3PW_{12}O_{40}$.xH_2O was added into a certain volume GO solution (2 mg/mL) to form solution A. 0.1398 g of KCl (0.1042 g of NH₄Cl) was put into 10 mL of water to form solution B. Then, the solution B was dropwise added into solution A at the rate of 1 mL/min under stirring and then the suspension was further stirred for 16 h (or 10 h). Finally, the suspension was transferred into a 25-mL Teflon-sealed autoclave for hydrothermal reaction at 120 °C for 8 h. After the autoclave was naturally cooled to room temperature, the suspension solution was centrifuged and washed until Cl^- was not detected, and then dried at 50 °C in vacuum. The chemical reaction equation as follows:

$$H_3[PW_{12}O_{40}] + 3KCl + xH_2O \rightarrow K_3[PW_{12}O_{40}] \bullet xH_2O + 3HCl \quad (1)$$

$$H_3[PW_{12}O_{40}] + 3NH_4Cl$$
$$+ xH_2O \rightarrow (NH_4)_3[PW_{12}O_{40}] \bullet xH_2O + 3HCl \quad (2)$$

Characterization

The crystal phase structure of prepared materials was recorded on a Bruker D8-advance A25X diffractometer (Germany) using a copper K_α radiation source (40 kV, 250 mA) in the 2θ range from 5 to 70°. Morphologies of them were observed on field emission scanning microscopy (FESEM, FEI, Nova, NanoSEM 450) and transmission electron microscopy (TEM, JEM-2100, JEOL, Tokyo, Japan). Fourier transform infrared spectra (FT-IR) of them were obtained on a Nicolet iS10 FT-IR spectrometer (Thermo Scientific, Germany) using KBr pellet technique over the wave number range of 4000–400 cm^{-1} with a resolution of 2 cm^{-1}. Raman spectra were measured by a Raman microspectrometer (Renishaw invia Raman Microscope, Britain) with a 514.5-nm laser. X-ray

photoelectron spectrum (XPS) measurements were performed on a PHI5000 Versaprobe scanning XPS microprobe (φULVAC-PHI Inc.) using the Al Kα line. The thermal property was examined using a thermal gravimetric analyzer (TGA, NETZSCH, TG209FI, Germany), in which the samples were heated from room temperature to 700 at 20 °C/min under a nitrogen flow. The photoluminescence emission spectra were recorded on an F-70000 fluorescence spectraphotometer (PL, Hitachi, Japan) at room temperature with the exciting light of wavelength 350 nm.

Photocatalytic activity test

In order to investigate the adsorption and photocatalytic performance of prepared materials for MO removal, photocatalytic activity tests were carried out in a photochemical reactor (Xujiang electro-mechanical plant, Nanjing, China). A 20-W UV lamp ($\lambda = 254$ nm) was put in the quartz immersion well with cooling coils to make the suspension at room temperature. In a typical experimental process, 0.0050 g of catalyst was put into a quartz tube containing 50.00 mL of MO solution (20 mg/L, C_0). Before UV light was switched on. The suspension was firstly stirred in dark for some time to make sure to reach the adsorption/desorption equilibrium and calculate adsorption removal rate (at this time, the MO concentration was set as C_q). Then, irradiation started and quartz tubes containing reaction suspensions were taken out at scheduled time intervals, immediately centrifuged at 4000 rpm for 10 min, and filtered through a 0.45-μm glass fiber filter to remove the catalyst particles (the MO concentrations were determined as C_t). MO samples were detected on UV-Vis spectrometer (detection wavelength was 463 nm); the standard curve for MO was linearly best fitted ($A = 0.0561C + 0.0006$, $R^2 = 0.9999$) with the concentration of MO varied from 1.0 to 20.0 mg/L.

The adsorption and photocatalytic degradation removal rates of MO over photocatalysts were calculated according to Eqs. 3 and 4, respectively.

$$\text{Removal rate by adsorption}(\%) = \frac{C_0 - C_q}{C_0} \times 100\% \qquad (3)$$

$$\text{Removal rate by photocatalytic degradation}(\%) = \frac{C_q - C_t}{C_0} \times 100\% \qquad (4)$$

In order to further assess the photocatalytic activity of KPW-RGO and NH₄PW-RGO, the experimental data were fitted by the pseudo-first-order model (Eq. (5)).

$$\ln \frac{C_t}{C_q} = -\kappa t \qquad (5)$$

The slope of the fitted line of ln (C_t/C_q) versus irradiation time is the rate constant (κ).

Results and discussion

Characterization of photocatalysts

Crystal phase of as-samples

In order to investigate the crystalline phase structure of prepared materials, the XRD patterns of GO, RGO, KPW, KPW-3RGO, NH₄PW, and NH₄PW-3RGO were recorded and are shown in Fig. 1. As seen in the picture, GO has a sharp and strong characteristic peak at $2\theta = 10.8°$ ascribed to (001) of GO, which disappears, and no obvious peak appears because of its low intensity. In order to observe it clearly, we inset a XRD pattern of RGO and a new weak characteristic peak of RGO at $2\theta = 24.5°$ can be observed after hydrothermal treatment in the solvent of ethanol-water (1:2) (Fig. 1, inset). This result implies that the GO may be reduced to RGO when ethanol was as a reductant in a hydrothermal environment (Luo et al. 2014b, Zhang et al. 2010). As for the XRD patterns of KPW, KPW-3RGO, NH₄PW, and NH₄PW-3RGO, we can see that all of them have the similar crystal phase at the atomic scale except that the peak intensities of KPW and NH₄PW are much stronger than those of KPW-3RGO and NH₄PW-3RGO, respectively. KPW, KPW-3RGO, NH₄PW, and NH₄PW-3RGO have major diffraction peaks located at $2\theta = 10.8°$, $15.2°$, $26.5°$, and $36.2°$, corresponding to $P_{12}W_{40}^{3-}$ (JCPDS no. 50-0305). However, the diffraction peak of RGO in two composites at 24.5° cannot be observed obviously, mainly because the diffraction intensity of RGO with low contents in composites is weak and the stack of RGO sheet has been suppressed by NH₄PW and KPW in the composites. The
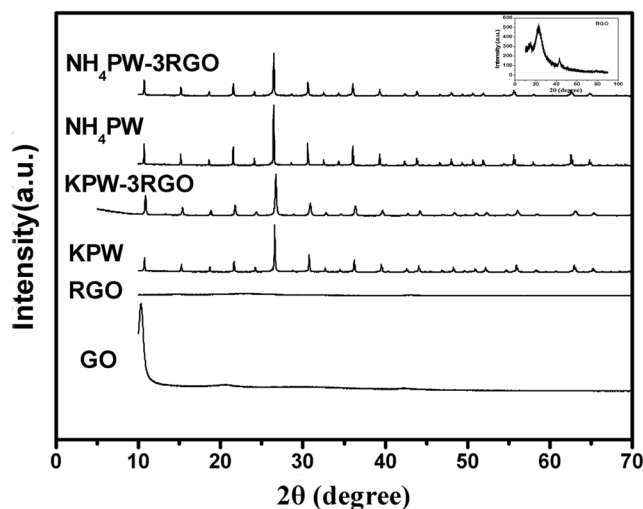

Fig. 1 XRD patterns of graphite oxide (GO), reduced graphene oxide (RGO), phosphotungstic acid potassium (KPW), phosphotungstic acid potassium 3wt%/reduced graphene oxide (KPW-3RGO), phosphotungstic acid ammonia (NH₄PW), and phosphotungstic acid ammonia 3 wt%/reduced graphene oxide (NH₄PW-3RGO). Inset picture is the XRD patterns of RGO

similar phenomenon can be seen in the 3-D TiO_2@RGO materials (Ding et al. 2016).

Morphology of as-samples

The microstructures of the prepared materials are studied by FESEM and TEM. Figures 2 and 3 show the FESEM of GO, RGO, KPW, NH_4PW, KPW-3RGO, and NH_4PW-3RGO. It can be seen that bare GO and RGO (Fig. 2a, b) have a flake-like structure with wrinkles, but RGO sheet is integrated and relatively smooth, whereas GO has an evident crack in the sheet. Figure 2c and d show the morphologies of bare KPW and NH_4PW materials, KPW materials are mono-dispersed spheres with some irregular pores in them and their diameters range from 500 to 800 nm, and the average diameter is about 600 nm (Fig. 2c). NH_4PW materials have a smooth spherical structure with a larger diameter than KPW ranging from 400 nm to 1.3 μm (Fig. 2d). As for the morphologies of KPW-3RGO and NH_4PW-3RGO, it is easy to find platelets of RGO sheets among the particles. But interestingly, most of mono-dispersed KPW spheres change into particles with smaller size; the diameter of KPW in KPW-3RGO ranges from 100 to 600 nm. The main reason may be that introduced RGO makes the irregular pores crack into particles (Fig. 2e, f). The resulting smaller particles will contact closely with reduced graphene oxide and provide more sites to target pollutants, which may make the KPW-3RGO composite have higher photocatalytic activity. As for NH_4PW-3RGO, smooth spherical structure of NH_4PW almost keeps in the NH_4PW-3RGO composite, but the size of them ranges from 250 to 400 nm, which is smaller than pure NH_4PW. The major reason maybe that the introduction of GO will suppress the growth of NH_4PW during the hydrothermal process; the similar experimental were results reported before (Li et al. 2017a, b). In all, the photocatalysts with a smaller size will necessarily result in good photocatalytic activity.

In order to further observe the microstructure of KPW-3RGO and NH_4PW-3RGO, the TEM images of them are provided in Fig. 3. Some of KPW particles in KPW-3RGO are larger blocks (Fig. 3a), but most of them become smaller particles with around 20-nm diameter and they are homogenously anchored onto the reduced graphene oxide with few layers (Fig. 3b). The NH_4PW components in NH_4PW-3RGO composites keep spherical structure with large size (100–600 nm, Fig. 3c), but their sizes are smaller than pure NH_4PW (400 nm–1.3 μm). Moreover, it is easy to see that the formation of heterojunction structures between NH_4PW and RGO (Fig. 3d), which will accelerate photo-induced interfacial charge transfer and result in better photocatalytic activity.

Fourier transform infrared and Raman spectra analysis

In order to obtain the functional groups information and reduction degree from GO to RGO in KPW-3RGO and NH_4PW-3RGO during the hydrothermal reaction, the Fourier transform infrared spectra of GO, RGO, KPW, KPW-3RGO, NH_4PW, and NH_4PW-3RGO materials were measured and are shown in Fig. 4a. It is clear that GO shows many absorption peaks corresponding to various oxygen functional groups such as –OH stretching vibrations (3443 cm^{-1}), overlapping peaks (1646 cm^{-1}) of C=O stretching vibration (1720 cm^{-1}) and C=C stretching vibration (1580 cm^{-1}), the epoxide C–O stretching vibrations (1135 cm^{-1}), and C–OH stretching vibrations (1069 cm^{-1}). After the reduction in the ethanol-water environment, the spectra of RGO has weaker absorption-peak intensities of the oxygen functional groups at 500–1700 cm^{-1} compared to those of GO, which indicates that the GO has been reduced to RGO greatly during hydrothermal process. As we know, the typical Keggin anion skeletal vibration bands are P–Oa, W–Ot, W–Ob–W, and W–Oc–W bonds. Among them, Oa is oxygen belongs to the central tetrahedral PO_4, Ob is the oxygen in W–Ob–W bridges between two different W_3O_{13} groups, Oc is the oxygen in W–Oc–W bridges of the same W_3O_{13} groups, and Ot is the terminal oxygens linked to a lone tungsten atom. From the FT-IR spectra of KPW, NH_4PW, KPW-3RGO, and NH_4PW-3RGO materials, we can see that 1080 cm^{-1} for asymmetric stretch vibration of P–Oa, 987 cm^{-1} due to asymmetric stretch vibration of W=Ot, 890 cm^{-1} for bending vibration of W–Ob–W, and 804 cm^{-1} for bending vibration of W–Oc–W, respectively (Essayem et al. 2001),which shows the presence of the $PW_{12}O_{40}^{3-}$ anion in these materials. There are also two broad absorption bands for KPW, NH_4PW, KPW-3RGO, and NH_4PW-3RGO at around 3443 cm^{-1} and 1643 cm^{-1} indexed to the ν (OH) and (δ), H_2O, respectively, which confirms that crystallization water exists in the KPW, NH_4PW, KPW-3RGO, and NH_4PW-3RGO materials. Besides these bands, the NH_4PW and NH_4PW-3RGO composite have two bands at around 1418 cm^{-1} and 3220 cm^{-1}, which are characteristic peaks of (δ)NH_4^+ ion and ν(N–H) (Corma et al. 1996). In all, the intensities of absorption bands of KPW-3RGO and NH_4PW-3RGO are weaker than those of KPW and NH_4PW, respectively, because of the existence of RGO. Raman spectroscopy is one of the most widely used techniques to understand the nature of the graphitic character in graphene-based materials. The Raman spectra of KPW, KPW-3RGO, NH_4PW, and NH_4PW-3RGO were recorded and shown in Fig. 4b. KPW and NH_4PW show Raman bands at 212, 233, 988, and 1003 cm^{-1} assigned to the Keggin structure of the $PW_{12}O_{40}^{3-}$ anion in pure KPW and NH_4PW materials (Holclajtner-Antunović et al. 2010, Liu et al. 2013). Compared with pure KPW and NH_4PW, the extra strong bands occurred at around 1605 cm^{-1}(G band) and 1348 cm^{-1} (D band) in KPW-3RGO and NH_4PW-3RGO composites; the D and G bands are common feature for sp^3 and sp^2 in-plane vibrations of bonded carbons of graphene (Rao et al. 2011), which indicated that the reduced graphene

Fig. 2 FESEM images of **a** graphite oxide (GO), **b** reduced graphene oxide (RGO), **c** phosphotungstic acid potassium (KPW), **d** phosphotungstic acid ammonia (NH₄PW), **e**, **f** phosphotungstic acid potassium 3 wt%/reduced graphene oxide (KPW-3RGO) and **g**, **h** phosphotungstic acid ammonia 3 wt%/reduced graphene oxide (NH₄PW-3RGO)
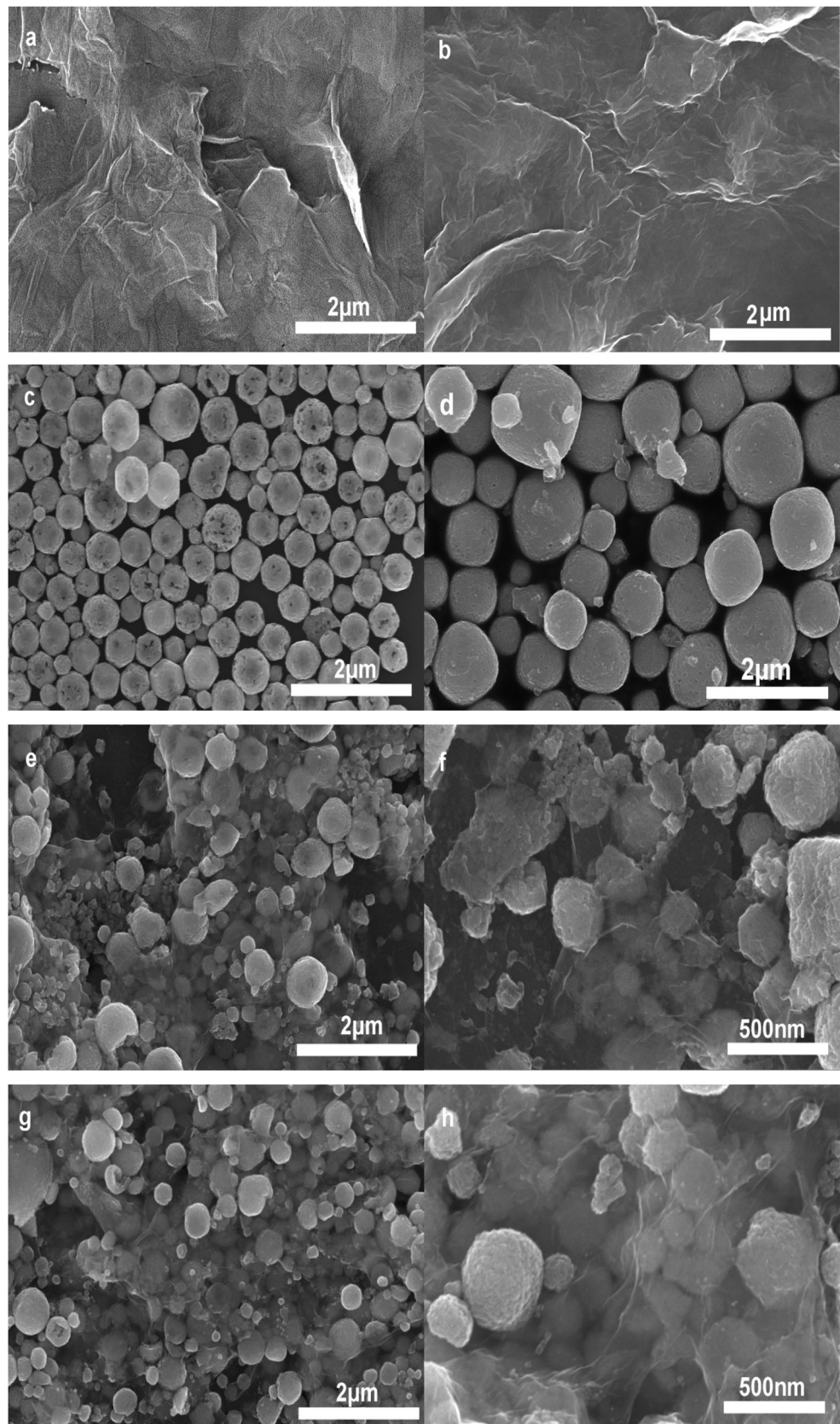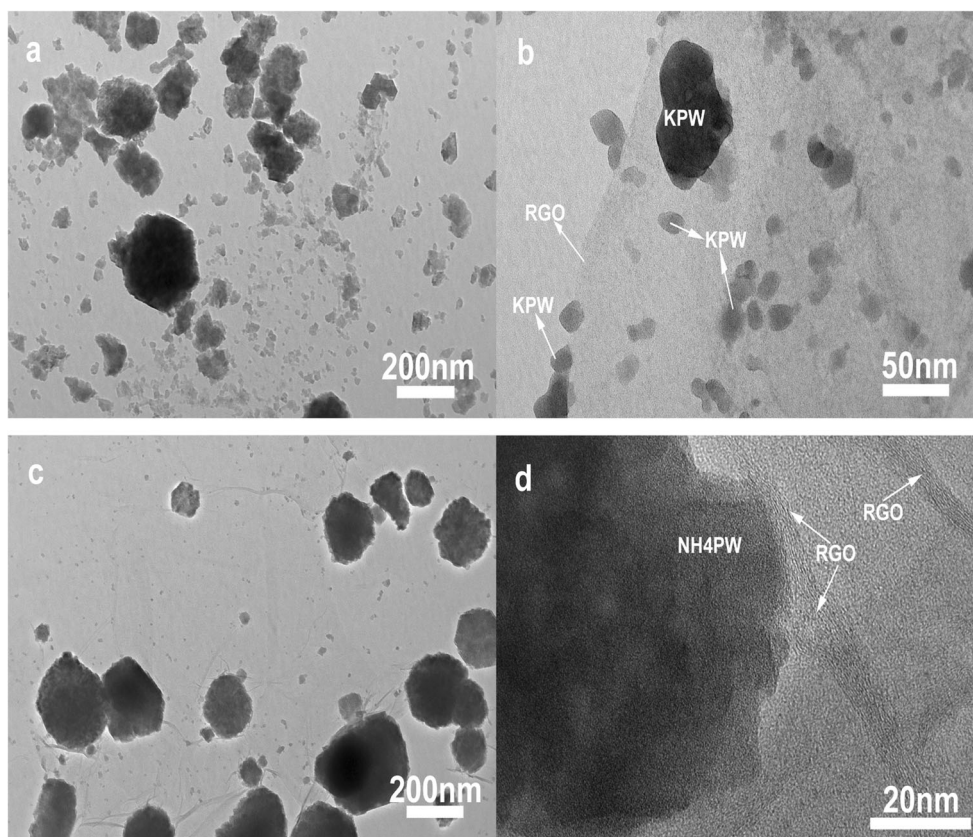
Fig. 3 TEM images of **a**, **b** phosphotungstic acid potassium 3 wt%/reduced graphene oxide (KPW-3RGO) and **c**, **d** phosphotungstic acid ammonia 3 wt%/reduced graphene oxide (NH$_4$PW-3RGO)

oxide exists in the composites and the results are similar to those in the F-TiO$_2$-10RGO composite we reported in our previous work (Luo et al. 2015).

X-ray photoelectron spectroscopy analysis

In order to further investigate chemical composition and element chemical states of as-samples, X-ray photoelectron spectroscopy (XPS) measurement for GO, KPW-3RGO, and NH$_4$PW-1RGO materials was performed and results are shown in Fig. 5. According to the XPS survey spectra (Fig. 5a), the KPW-3RGO and NH$_4$PW-1RGO composites contain W, O, P, and C elements corresponding to the binding energies of W4f, W4d, W4p, W4s, O1s, P2s, P2p, and C1s. Besides those elements, KPW-3RGO and NH$_4$PW-1RGO contain K and N corresponding to K2p, K2s, and N1s, respectively. Figure 6b is the C1s spectra comparison of GO, KPW-3RGO, and NH$_4$PW-1RGO. The main C1s peaks for GO located at 287.3 eV and 284.3 eV belong to oxygen-containing groups (C−OH/C=O/C(O)O) and C−C/C=C/H–C bonds of Sp^2 carbon of GO, respectively (Luo et al. 2015). The peaks of KPW-3RGO and NH$_4$PW-1RGO at 287.3 eV exist, but their intensities obviously weaken compared to GO, which indicates that GO has been partly transformed to graphene after hydrothermal treatment. The similar result was obtained in the previous work (Xia et al. 2017).

Figure 5c is the O1s spectra comparison of GO, KPW-3RGO, and NH$_4$PW-1RGO; the O1s peak of GO around 532 eV is ascribed to C–O and C=O. The O1s peaks of KPW-3RGO and NH$_4$PW-1RGO are around 530.9 eV and 530.6 eV, which correspond to inorganic O bond (P–O and W–O) and residue oxygen-containing groups (C–O and C=O). Two composites have same signals; the peak at 36.6 eV is ascribed to W4f, and the peak at 135 eV can be ascribed to P2p (Fig. 5d, e) (Li et al. 2017a, b). KPW-3RGO has a peak located at 293.1 which is indexed to the K2p (Fig. 5f) and the N1s features peak of NH$_4$PW-1RGO locates at 402.1 eV (Fig. 5g). The peaks extend from 400.3 to 403.6 eV. There is no N-doped TiO$_2$ because there is no peak located at 399.5 eV attributed to N-TiO$_2$. The above XPS analysis results show that the KPW-3RGO and NH$_4$PW-1RGO materials have been successfully prepared and GO can be reduced to RGO by ethanol in the hydrothermal environment greatly.

PL analysis

The photoluminescence (PL) spectra are related to the transfer behavior of the photo-produced electrons and holes so that it can reflect the separation and recombination of the electron-hole pair inside the semiconductors. Figure 6 shows the PL spectra of KPW, KPW-3RGO, NH$_4$PW, and NH$_4$PW-3RGO
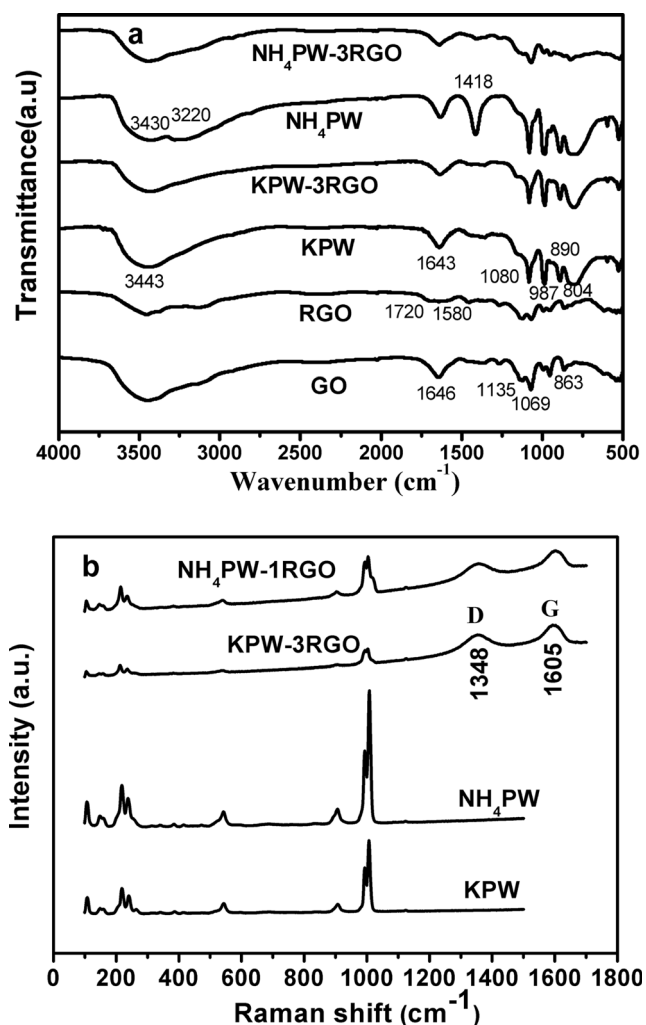
Fig. 4 FT-IR spectra of graphite oxide (GO), reduced graphene oxide (RGO), phosphotungstic acid potassium (KPW), phosphotungstic acid potassium 3 wt%/reduced graphene oxide (KPW-3RGO), phosphotungstic acid ammonia (NH_4PW), and phosphotungstic acid ammonia 3 wt%/reduced graphene oxide (NH_4PW-3RGO) materials (**a**) and Raman spectra of phosphotungstic acid potassium (KPW), phosphotungstic acid potassium 3wt %/reduced graphene oxide (KPW-3RGO), phosphotungstic acid ammonia (NH_4PW), and phosphotungstic acid ammonia 1 wt%/reduced graphene oxide (NH_4PW-1RGO) (**b**)

materials. As can be seen in Fig. 6, the four materials exhibit the same sharp emission bands at about 469 nm when the excitation wavelength is 350 nm. The PL intensity of KPW-3RGO is weaker than that of KPW, and the NH_4PW-3RGO has weaker PL intensity than NH_4PW, which indicates that the recombination of electron-hole produced on the surface of two composites reduces compared with counterpart pure KPW and NH_4PW. The introduction of RGO into KPW and NH_4PW effectively suppress the recombination of electron-hole pair because the RGO can transfer electron produced from the conduction band of pure KPW and NH_4PW. The effective suppression of the electron-hole produced on the KPW-3RGO and NH_4PW-3RGO will improve the photocatalytic activity greatly.

Thermogravimetric analysis

In order to investigate the thermal stability of as-samples, thermogravimetric analysis of RGO, KPW, KPW-3RGO, NH_4PW, and NH_4PW-RGO was performed and results are shown in Fig. 7. KPW and NH_4PW lose water up to 100 °C in a single step followed by a mass loss which corresponds to adsorbed and crystallization water molecules. The weight loss ratio for KPW is only 2.82 wt% and there is no obvious second mass loss for KPW between 450 to 620 °C, which indicates that KPW has no protons and its chemical formula must be $K_3P_{12}W_{40}$ (Holclajtner-Antunović et al. 2010). In the case of NH_4PW, there is another obvious mass loss from 450 to 620 °C, and the weight loss ratios of NH_4PW at 20–100 °C and 450–620 °C are 2.26 wt% and 2.43 wt%, respectively. As for KPW-3RGO and NH_4PW-1RGO, except for the above weight loss, it clearly shows rapid decomposition of the oxygen-containing groups of RGO at about 200 °C in these two composites compared to those of pure KPW and NH_4PW (He et al. 2013, Zhang and Choi 2012), which indicates that GO has not completely been reduced to graphene. The weight loss ratios of NH_4PW-1RGO at 20–100 °C, 100–450 °C, and 450–620 °C are 3.0 wt%, 1.69 wt%, and 5.13 wt%, and the weight loss ratios of KPW-3RGO at 20–100 °C, 100–450 °C, and 450–620 °C are 3.35 wt%, 3.89 wt%, and 3.85 wt%, respectively. Comparatively, the weight loss ratios of RGO at 20–100 °C, 200–450 °C, and 450–620 °C are 19.0 wt% and 5.2 wt%, which indicates that RGO has the evaporation of water molecules around 100 °C and rapid decomposition of the oxygen-containing groups from 200 to 620 °C. The above weight loss analysis indicates that GO is transformed to RGO partly.

Adsorption and photocatalytic performance

Adsorption equilibrium experiment

In the whole photocatalytic degradation process, adsorption, photocatalytic degradation, and photolysis may have specific contributes to the removal of target pollutants. As the photocatalytic reactions predominantly occur on the surface of catalysts, adsorption abilities of KPW-3RGO and NH_4PW-RGO towards MO are key factors that can affect their photocatalytic efficiency. Therefore, it is necessary to determine adsorption equilibrium time and comprehend the contribution of adsorption ability to photocatalytic activity. Under the experiment condition (0.6 g/L for KPW-3RGO and KPW, 0.4 g/L for NH_4PW-RGO and NH_4PW), MO adsorption experiments (20 mg/L MO solution, pH 4.0) were carried out and the results are shown in Fig. 8. We can see from Fig. 8 that the adsorption removal ratios of MO on KPW and NH_4PW increases gradually and reaches adsorption equilibrium of less than 60 min. Adsorption removal rates of MO over KPW and
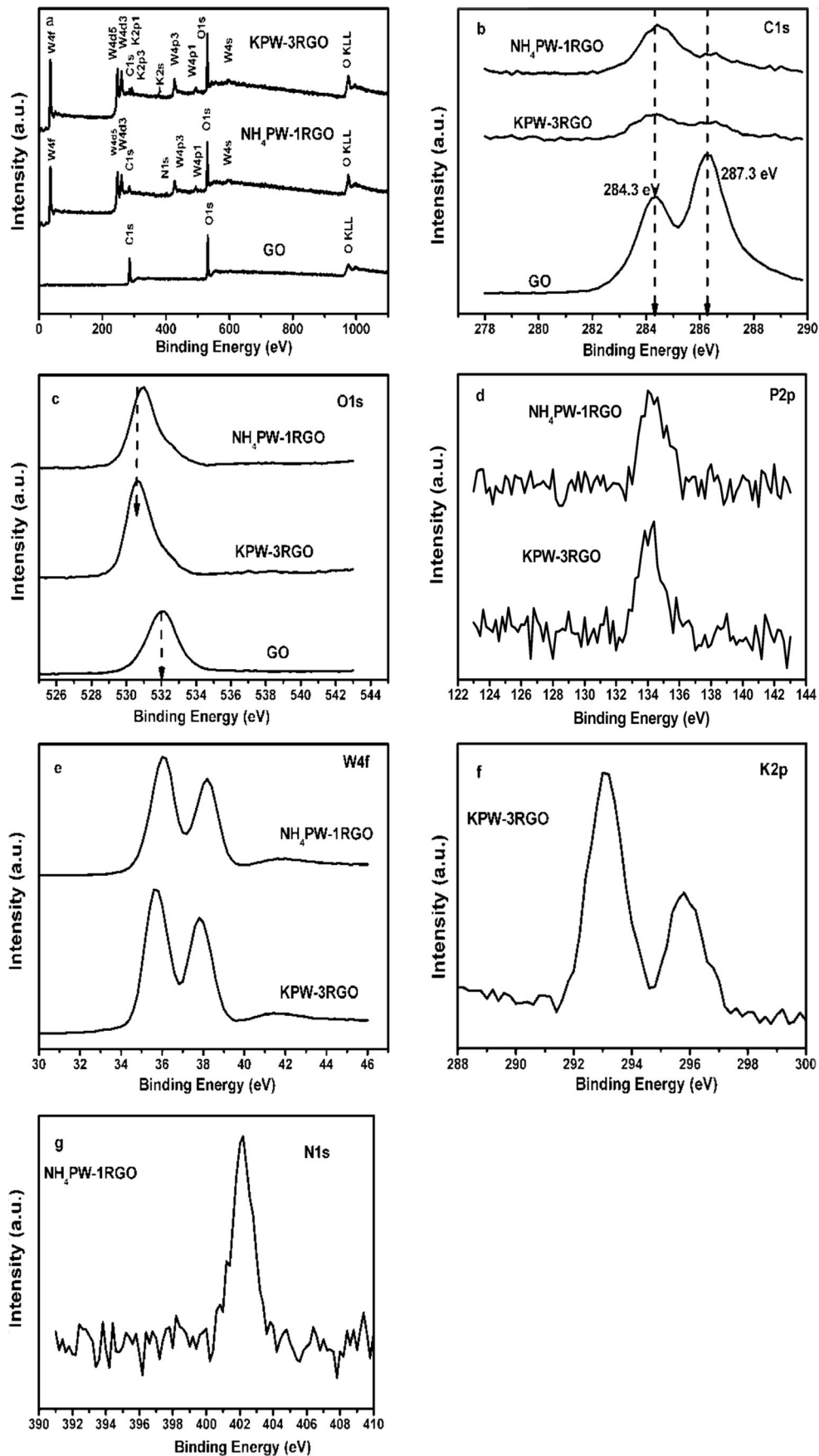
◀ **Fig. 5.** XPS survey spectra of graphite oxide (GO), phosphotungstic acid potassium 3 wt%/reduced graphene oxide (KPW-3RGO), and phosphotungstic acid ammonia 1 wt%/reduced graphene oxide (NH₄PW-1RGO) (**a**). C1s and O1s spectra comparison of graphene oxide (GO), phosphotungstic acid potassium 3 wt%/reduced graphene oxide (KPW-3RGO), and phosphotungstic acid ammonia 1 wt%/ reduced graphene oxide (NH₄PW-1RGO) (**b**, **c**), P2p (**d**), and W4f (**e**) spectra comparison of phosphotungstic acid potassium 3 wt%/reduced graphene oxide (KPW-3RGO) and phosphotungstic acid ammonia1 wt%/reduced graphene oxide (NH₄PW-1RGO), K2p (**f**) and N1s (**g**) spectra of phosphotungstic acid potassium 3 wt%/reduced graphene oxide (KPW-3RGO) and phosphotungstic acid ammonia 1 wt%/reduced graphene oxide (NH₄PW-1RGO), respectively

NH₄PW are 5.39% and 4.15%, respectively, which implies that the KPW and NH₄PW materials have little adsorption ability for MO, which may result in low transferring rate for MO from solution to the surface of catalysts. However, after RGO sheets are introduced into these two catalysts, adsorption removal rates of MO on KPW-3RGO and NH₄PW-1RGO roar to 19.6 % and 12.0 % in the first 10 min, respectively, and the adsorption equilibriums have been established by 30 min. The result indicates that the RGO in the composites has strong adsorption ability and rapid adsorption rate for MO, which will enhance the transferring rate of MO from solution to the surface of catalysts and then improve the photocatalytic activity. In order to make sure that the adsorption equilibrium has been established, adsorption time in the dark for all the prepared materials will be set at 120 min.

Optimization of RGO mass contents in KPW-RGO and NH₄PW-RGO composites

Based on the above adsorption analysis, we can see that RGO in the composites will play a significantly important role in
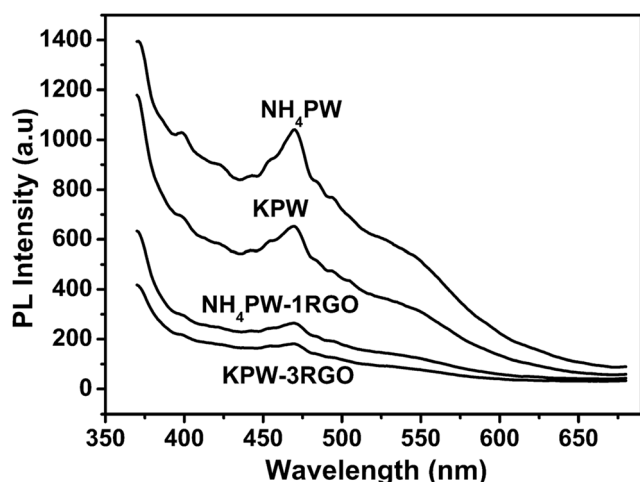
Fig. 7 Thermo-gravimetric analysis for phosphotungstic acid potassium (KPW), phosphotungstic acid potassium 3 wt%/reduced graphene oxide (KPW-3RGO), phosphotungstic acid ammonia (NH₄PW), and phosphotungstic acid ammonia 1 wt%/reduced graphene oxide (NH₄PW-1RGO)
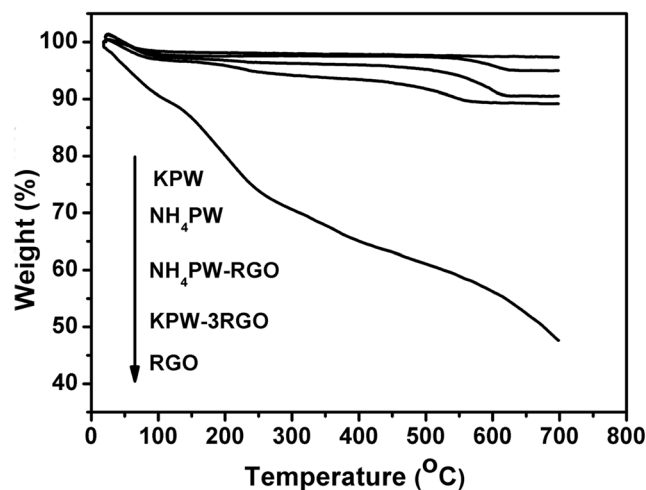
removing MO. Therefore, it is necessary to optimize the amount of RGO in KPW-RGO and NH₄PW-RGO composites. The adsorption and photocatalytic degradation time course of MO over a series of KPW-RGO and NH₄PW-RGO samples with different RGO contents are shown in Fig. 9. We can see that adsorption removal rates of MO on KPW-1RGO, KPW-3RGO, and KPW-5RGO are 9.05%, 29.63%, and 39.36%, respectively (Fig. 9a). The adsorption removal rates of MO on KPW-RGO go up rapidly from 9.05 to 39.36% with the increasing mass ratios of RGO from 1.0 to 5.0% in the composites. Photocatalytic degradation removal rates of MO on KPW-1RGO, KPW-3RGO, and KPW-5RGO are 58.16%, 66.33%, and 44.67%, and the total removal rates of MO on them are 67.21%, 95.96%, and 84.03%,
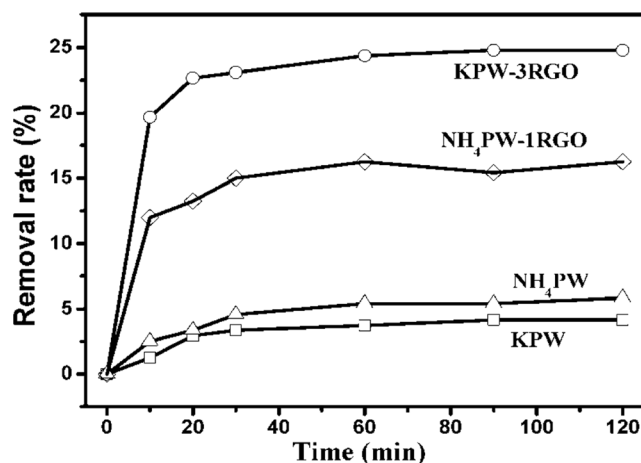
Fig. 6 Photoluminescence spectra of phosphotungstic acid potassium (KPW), phosphotungstic acid potassium 3wt %/reduced graphene oxide (KPW-3RGO), phosphotungstic acid ammonia (NH₄PW), and phosphotungstic acid ammonia 1 wt%/reduced graphene oxide (NH₄PW-1RGO)

Fig. 8 Adsorption removal of MO on phosphotungstic acid potassium (KPW), phosphotungstic acid potassium 3 wt%/reduced graphene oxide (KPW-3RGO), phosphotungstic acid ammonia (NH₄PW), and (phosphotungstic acid ammonia 1 wt%/reduced graphene oxide (NH₄PW-1RGO) materials
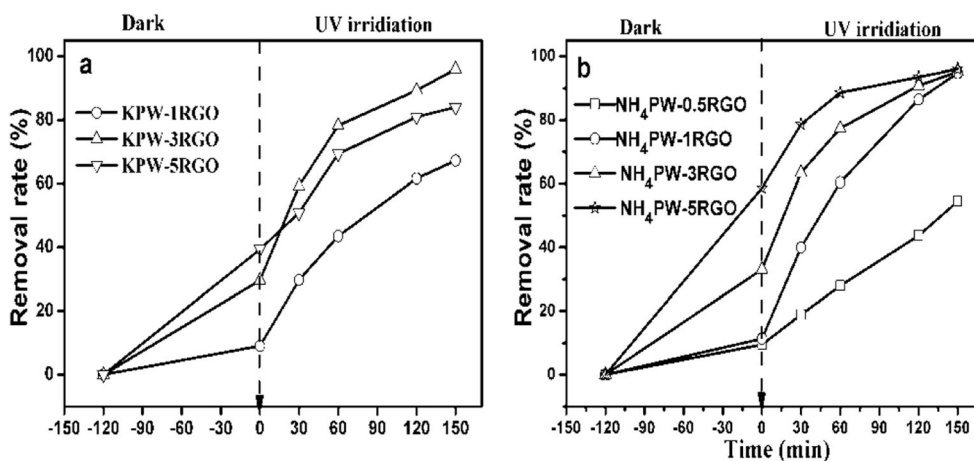
Fig. 9 Time course of the adsorption and photocatalytic degradation removal rate of MO (initial concentration 20 mg/L, pH 4.0) over phosphotungstic acid potassium 1 wt%/reduced graphene oxide (KPW-1RGO), phosphotungstic acid potassium 3 wt%/reduced graphene oxide (KPW-3RGO), and phosphotungstic acid potassium 5 wt%/reduced graphene oxide (KPW-5RGO) (**a**, catalyst dosage 0.6 g/L) and

phosphotungstic acid ammonia 0.5 wt%/reduced graphene oxide (NH_4PW-0.5RGO), phosphotungstic acid ammonia 1 wt%/reduced graphene oxide (NH_4PW-1RGO), phosphotungstic acid ammonia 3 wt%/reduced graphene oxide (NH_4PW-3RGO), and phosphotungstic acid ammonia 5 wt%/reduced graphene oxide (NH_4PW-5RGO) (**b**, 1.0 g/L). The arrow indicates the beginning of UV light irradiation

respectively. From the view of photocatalytic degradation and total removal rates of MO, the optimal mass ratio of RGO in KPW-RGO is 3.0 wt%. As for the NH_4PW-RGO composites, adsorption removal rates of MO on the NH_4PW-0.5RGO, NH_4PW-1RGO, NH_4PW-3RGO, and NH_4PW-5RGO are 9.44%, 11.30%, 33.03%, and 58.67%, respectively. The adsorption removal rates of MO on NH_4PW-RGO roar from 9.44% to 58.67% with the increasing mass ratios of RGO from 0.5 to 5.0 wt% in the composites. Photocatalytic degradation removal rates of MO on NH_4PW-0.5RGO, NH_4PW-1RGO, NH_4PW-3RGO, and NH_4PW-5RGO are 45.04%, 83.44%, 62.16%, and 37.38%, and the total removal rates of MO on them are 54.48%, 94.74%, 95.18%, and 96.05%, respectively (Fig. 9b). From the view of photocatalytic degradation removal rate, the optimal mass ratio of RGO to NH_4PW-RGO is 1.0 wt% for MO removal.

The evaluation of photocatalytic activity

In order to compare the photocatalytic activity of two prepared phosphotungstic acid salts/reduced graphene oxide composites under optimal degradation conditions and investigate the role of RGO in two composites, the photocatalytic degradation of MO over KPW, KPW-3RGO, NH_4PW, and NH_4PW-1RGO, and photolysis of MO was carried out and the results are shown in Fig. 10. The optimal degradation conditions of MO over KPW and KPW-3RGO are 20 mg/L MO initial concentration, 0.6 g/L dosage, and pH value of 4.0. The optimal degradation conditions of MO over NH_4PW, and NH_4PW-1RGO are 20 mg/L MO initial concentration, 1.0 g/L dosage, and pH value of 4.0. The adsorption removal rates of MO on the KPW, KPW-3RGO, NH_4PW, and NH_4PW-1RGO are 6.35%, 29.63%, 4.48%, and 11.30%, respectively. Photocatalytic degradation removal rates

of MO on KPW, KPW-3RGO, NH_4PW, and NH_4PW-1RGO are 37.58%, 67.23%, 68.32%, and 83.44% and the total removal rates of MO on them are 43.93%, 96.86%, 72.80%, and 94.74%, respectively. The total removal ratio of photolysis is only 11.55% (Fig. 10a). The contributions of RGO to the total removal rates of MO are 52.93% and 21.88% in KPW-3RGO and NH_4PW-1RGO. Among them, the contributions of total RGO in KPW-3RGO and NH_4PW-1RGO to photocatalytic degradation removal rates are 26.35% and 15.12%. However, the RGO content in KPW-3RGO is 3 times that in NH_4PW-1RGO. Therefore, the contribution efficiency RGO in NH_4PW-1RGO is better than that in KPW-3RGO. Figure 10b shows that the kinetic rate constant of MO over KPW-3RGO (0.01989 min^{-1}) is 5.42 times of that of KPW (0.00367 min^{-1}), and NH_4PW-1RGO (0.0184 min^{-1}) is 2.26 times of that of NH_4PW (0.00814 min^{-1}). The rate constant of photolysis is only 8.4×10^{-4}. The enhanced photocatalytic activity is ascribed to photo-induced interfacial charge transfer on the heterojunction between RGO and NH_4PW or KPW and strong adsorption ability of RGO towards MO. In addition, the total RGO amount in KPW-3RGO plays a much more important role in enhancing the pure KPW than that in NH_4PW-1RGO. The major reason may be that KPW particles are much smaller than pure KPW because the introduced RGO into KPW-3RGO makes the KPW crack and RGO has better contact with smaller KPW (seen in Fig. 3 TEM). Compared with the HPW-RGO (0.00892 min^{-1}) which was reported in the previous work (Xia et al. 2017), the KPW-3RGO and NH_4PW-1RGO composites have extraordinary excellent photocatalytic activity.

The recyclable experiment

In order to investigate the photochemical stability of the prepared KPW-3RGO and NH_4PW-1RGO photocatalyst, the
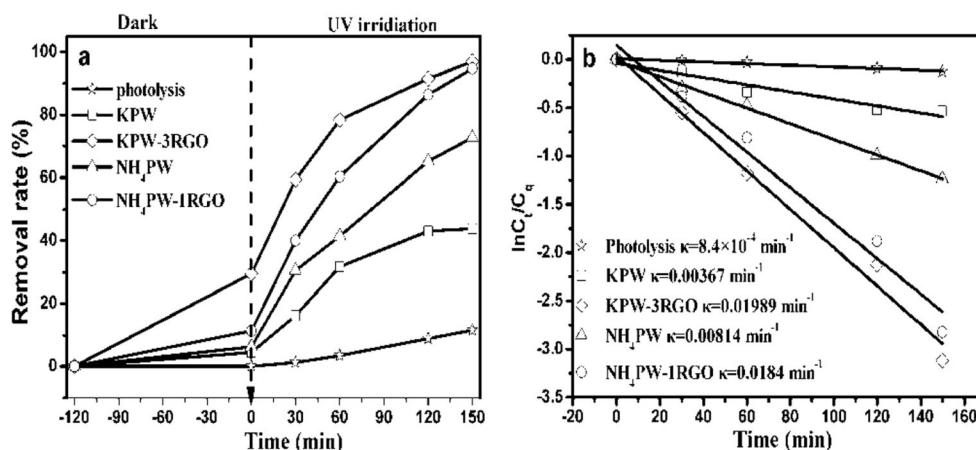
Fig. 10 Direct photolysis (20 W UV light, main wavelength 254 nm) and adsorption and photocatalytic decomposition time courses of MO (initial concentration 10 mg/L) on KPW (phosphotungstic acid potassium), phosphotungstic acid potassium 3 wt%/reduced graphene oxide (KPW- 3RGO, 0.6 g/L), phosphotungstic acid ammonia (NH_4PW), and phosphotungstic acid ammonia 1 wt%/reduced graphene oxide (NH_4PW-1RGO, 1.0 g/L) (**a**) and the corresponding first-order plots (**b**)

repeated experiments were carried out and are shown in Fig. 11. After each photocatalytic reaction, the photocatalyst was centrifuged and washed by anhydrous alcohol for reuse and then the next cycle started with initial MO concentration of 20 mg/L. We can see that after three cycles, the removal rates of MO on KPW-3RGO photocatalyst decrease from 89.19 to 63.77%, and the removal rates of MO over NH_4PW-1RGO photocatalyst decrease from 90.48 to 49.98%. The experiment results show that the removal rate of MO on two composites decrease gradually because MO has not been removed after the first cycle finishes (for this kind of composites, the decoloration rate does not reach 100% even although the degradation time is lengthened) and the residue MO on the catalyst surface is still into next cycle even after washing with ethanol. Moreover, it is possible that the reduced graphene oxide sheet can be photocatalytically degraded by KPW and

NH_4PW, which also make the photocatalytic activity of composites decrease (Akhavan et al. 2010). In all, the results suggest that the two composites can be separated via centrifugation and it can be reused even if the stability of photocatalytic performance will decrease with the increasing of reuse time compared to polyoxometalates/RGO reported in the references.

Conclusion

In conclusion, in order to improve recyclability, stability, and the photocatalytic activity of polyoxometalates, we successfully prepared two kinds of KPW-3RGO and NH_4PW-1RGO composites via hydrothermal treatment. The crystal phase structure, morphology, and chemical composition of them were comparatively investigated in detail. The result shows that the prepared materials have extraordinary excellent photocatalytic activity and good adsorption ability for MO. The enhanced photocatalytic activity is ascribed to photo-induced interfacial charge transfer on the heterojunction between RGO and NH_4PW or KPW and strong adsorption ability of RGO towards MO. In addition, the total RGO amount in KPW-3RGO plays a much more important role in enhancing photocatalytic activity of pure KPW than that in NH_4PW-1RGO. Most importantly, KPW-3RGO and NH_4PW-1RGO have excellent recyclability and relatively good stability compared with polyoxometalates/RGO, which cannot be reused.
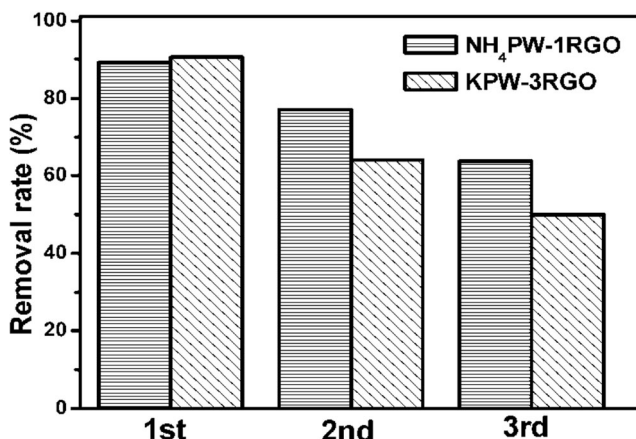

Fig. 11 Recycled degradation of MO over phosphotungstic acid potassium 3 wt%/reduced graphene oxide (KPW-3RGO) and phosphotungstic acid ammonia 3 wt%/reduced graphene oxide (NH_4PW-1RGO)

References

Akhavan O, Abdolahad M, Esfandiar A, Mohatashamifar M (2010) Photodegradation of graphene oxide sheets by TiO_2 nanoparticles after a photocatalytic reduction. J Phys Chem C 114:12955–12959

Antoniadis A, Takavakoglou V, Zalidis G, Darakas E, Poulios I (2010) Municipal wastewater treatment by sequential combination of photocatalytic oxidation with constructed wetlands. Catal Today 151: 114–118

Chowdhury S, Balasubramanian R (2014) Graphene/semiconductor nanocomposites (GSNs) for heterogeneous photocatalytic decolorization of wastewaters contaminated with synthetic dyes: a review. Appl Catal B Environ 160–161:307–324

Corma A, Martinez A, Martinez C (1996) Acidic Cs^+, NH_4^+, and K^+ salts of 12-tungstophosphoric Acid as solid catalysts for isobutane/2-butene alkylation. J Catal 164:422–432

Ding Y, Bai W, Sun J, Wu Y, Memon MA, Wang C, Liu CB, Huang Y, Geng JX (2016) Cellulose tailored anatase TiO_2 nanospindles in three-dimensional graphene composites for high-performance supercapacitors. ACS Appl Mater Interfaces 8:12165–12175

Essayem N, Holmqvist A, Gayraud PY, Vedrine JC, Ben Taarit Y (2001) In situ FTIR studies of the protonic sites of $H_3PW_{12}O_{40}$ and its acidic cesium salts $M_xH_{3-x}PW_{12}O_{40}$. J Catal 197:273–280

Feng C, Li Y, Liu X (2012) hotocatalytic degradation of imidacloprid by phosphotungstic acid supported on a mesoporous sieve MCM-41. Chin. J. Chem 30:127–132

He Y, Liu Y, Wu T, Ma J, Wang X, Gong Q, Kong W, Xing F, Liu Y, Gao J (2013) An environmentally friendly method for the fabrication of reduced graphene oxide foam with a super oil absorption capacity. J Hazard Mater 260:796–805

Holclajtner-Antunović I, Mioč UB, Todorović M, Jovanović Z, Davidović M, Bajuk-Bogdanović D, Laušević Z (2010) Characterization of potassium salts of 12-tungstophosphoric acid. Mater Res Bull 45:1679–1684

Hori H, Yamamoto A, Koike K, Kutsuna S, Murayama M, Yoshimoto A, Arakawa R (2008) Photocatalytic decomposition of a perfluoroether carboxylic acid by tungstic heteropolyacids in water. Appl Cataly B: Environ 82:58–66

Hummers WSOR (1958) Preparation of graphitic oxide. J Am Chem Soc 80:1339

Ji TH, Sun M, Han P (2014) A review of the preparation and applications of graphene/semiconductor composites. Carbon 70:319

Kanakaraju D, Glass BD, Oelgemöller M (2013) Titanium dioxide photocatalysis for pharmaceutical wastewater treatment. Environ Chem Lett 12:27–47

Khai TV, Kwak DS, Kwon YJ, Cho HY, Huan TN, Chung H, Ham H, Lee C, Dan NV, Tung NT, Kim HW (2013) Direct production of highly conductive graphene with a low oxygen content by a microwave-assisted solvothermal method. Chem Eng J 232:346–355

Kooti M, Kooshki F, Nasiri E, Sedeh AN (2018) $H_3PW_{12}O_{40}$ anchored on graphene-grafted silica-coated $MnFe_2O_4$ as magnetic catalyst for Mannich reaction. J. Iranian. Chem Soc 15:943–953

Kormali P, Troupis A, Triantis T, Hiskia A, Papaconstantinou E (2007) Photocatalysis by polyoxometallates and TiO_2: a comparative study. Catal Today 124:149–155

Li H, Liu X, Qi S, Xu LL, Shi GS, Ding YH, Yan XY, Huang Y, Geng JX (2017a) Graphene oxide facilitates solvent-free synthesis of well-dispersed, faceted zeolite crystals. Angew Chem Int Ed 129: 14090–14095

Li X, Xue H, Pang H (2017b) Facile synthesis and shape evolution of well-defined phosphotungstic acid potassium nanocrystals as a highly efficient visible-light-driven photocatalyst. Nanoscale 9:216–222

Linsebigler AL, Lu GQ, Yates JT (1995) Photocatalysis on TiO_2 surfaces-principles, mechanism, and selected results. Chem Rev 95:735–758

Liu K, Chen T, Hou Z, Wang Y, Dai L (2013) Graphene oxide as support for the immobilization of phosphotungstic acid: application in the selective oxidation of benzyl alcohol. Catal Lett 144:314–319

Liu CG, Zheng T, Liu S, Zhang HY (2016) Photodegradation of malachite green dye catalyzed by Keggin-type polyoxometalates under visible-light irradiation: Transition metal substituted effects. J Mol Struct 1110:44–52

Luo G, Kang L, Zhu M, Dai B (2014a) Highly active phosphotungstic acid immobilized on amino-functionalized MCM-41 for the oxidesulfurization of dibenzothiophene. Fuel Process Technol 118: 20–27

Luo LJ, Zhang XJ, Ma FJ, Zhang AL, Bian LC, Pan XJ, Jiang FZ (2014b) Photocatalytic degradation of bisphenol A by TiO_2-reduced graphene oxide nanocomposites. React Kinet Mech Catal 114(1): 311–322

Luo L, Yang Y, Zhang A, Wang M, Liu Y, Bian L, Jiang F, Pan X (2015) Hydrothermal synthesis of fluorinated anatase TiO_2/reduced graphene oxide nanocomposites and their photocatalytic degradation of bisphenol A. Appl Surf Sci 353:469–479

Marsolek MD, Kirisits MJ, Gray KA, Rittmann BE (2014) Coupled photocatalytic-biodegradation of 2,4,5-trichlorophenol: effects of photolytic and photocatalytic effluent composition on bioreactor process performance, community diversity, and resistance and resilience to perturbation. Water Res 50:59–69

Méndez L, Torviso R, Pizzio L, Blanco M (2011) 2-Methoxynaphthalene acylation using aluminum or copper salts of tungstophosphoric and tungstosilicic acids as catalysts. Catal Today 173:32–37

Meyer JC, Geim AK, Katsnelson MI, Novoselov KS, Booth TJ, Roth S (2007) The structure of suspended graphene sheets. Nature 446:60–63

Moniz SJA, Shevlin SA, Martin DJ, Guo ZX, Tang J (2015) Visible-light driven heterojunction photocatalysts for water splitting-a critical review. Energy Environ Sci 8:731–759

Morales-Torres S, Pastrana-Martinez LM, Figueiredo JL, Faria JL, Silva AM (2012) Design of graphene-based TiO_2 photocatalysts-a review. Environ Sci Pollut Res Int 19:3676–3687

Pelaez M, Nolan NT, Pillai SC, Seery MK, Falaras P, Kontos AG, Dunlop PSM, Hamilton JWJ, Byrne JA, O'Shea K, Entezari MH, Dionysiou DD (2012) A review on the visible light active titanium dioxide photocatalysts for environmental applications. Appl Catal B Environ 125:331–349

Rao R, Podila R, Tsuchikawa R, Katoch J, Tishler D, Rao A, Ishigami M (2011) Effects of layer stacking on the combination Raman modes in graphene. ACS Nano 5:1594–1599

Stankovich S, Dikin DA, Dommett GHB, Kohlhaas KM, Zimney EJ, Stach EA, Piner RD, Nguyen ST, Ruoff RS (2006) Graphene-based composite materials. Nature 442:282–286

Troupis A, Triantis TM, Gkika E, Hiskia A, Papaconstantinou E (2009) Photocatalytic reductive–oxidative degradation of Acid Orange 7 by polyoxometalates. Appl Catal B Environ 86:98–107

Wang XS, Huang YB, Lin ZJ, Cao R (2014) Phosphotungstic acid encapsulated in the mesocages of amine-functionalized metal-organic frameworks for catalytic oxidative desulfurization. Dalton Trans 43: 11950–11958

Xia LH, Luo LJ, Li J, Fan Y, Tan W, Yang WR, Wang HB, Shu L (2017) The preparation and photocatalytic activity of phosphotungstic acid-reduced graphene oxide composites. Desalin Water Treat 96:178–185

Xiao J, Wu L, Wu Y, Liu B, Dai L, Li Z, Xia Q, Xi H (2014) Effect of gasoline composition on oxidative desulfurization using a

phosphotungstic acid/activated carbon catalyst with hydrogen peroxide. Appl Energy 113:78–85

Xu J, Wang L, Zhu Y (2012) Decontamination of bisphenol A from aqueous solution by graphene adsorption. Langmuir 28:8418–8425

Yang J, Chen D, Zhu Y, Zhang Y, Zhu Y (2017) 3D-3D porous Bi_2WO_6/graphene hydrogel composite with excellent synergistic effect of adsorption-enrichment and photocatalytic degradation. Appl Catal B: Environ 205:228–237

Zhang WL, Choi HJ (2012) Silica-graphene oxide hybrid composite particles and their electroresponsive characteristics. Langmuir 28:7055–7062

Zhang Y, Tang ZR, Fu X, Xu YJ (2010) TiO_2-graphene nanocomposites for gas-phase photocatalytic degradation of volatile aromatic pollutant-Is TiO_2-graphene truly different from other TiO_2-carboncomposite materials? ACS Nano 4:7303–7314

Zhang L, Li S, Zhang Z, Tan L, Pang H, Ma H (2017) Facile fabrication of reduced graphene oxide and Keggin-type polyoxometalates nanocomposite film for high performance electrocatalytic oxidation of nitrite. J Electroanal Chem 807:97–103

Zhao L, Chi Y, Yuan Q, Li N, Yan W, Li X (2013) Phosphotungstic acid anchored to amino-functionalized core-shell magnetic mesoporous silica microspheres: a magnetically recoverable nanocomposite with enhanced photocatalytic activity. J Colloid Interface Sci 390:70–77

Zhu Y, Zhu M, Kang L, Yu F, Dai B (2015) Phosphotungstic acid supported on mesoporous graphitic carbon nitride as catalyst for oxidative desulfurization of fuel. Ind Eng Chem Res 54:2040–2047